Design and Closed-loop Control of a Tri-layer Polypyrrole based Telescopic Soft Robot

Mohamed Taha Chikhaoui, Amélie Cot, Kanty Rabenorosoa, Patrick Rougeot, and Nicolas Andreff

***Abstract*— A novel structure of a 2 DoF telescopic soft robot using a tri-layer Polypyrrole (PPy) soft micro-actuator with deployment is presented in this paper. The kinematic model is introduced and the Position Based Visual Servo (PBVS) control with path-planning and obstacle avoidance algorithms is developed. A prototype is presented and the control schemes are validated experimentally. A satisfactory accuracy with a sub-millimetric positioning error is obtained namely 287.6 microns for a circular path and 210 microns for obstacle avoidance.**

I. INTRODUCTION

The navigation in confined zones and/or constrained environments has always been a remarkable challenge for robotic researchers. Should it be for undersea applications, spray-painting, rescue, or even inside power plants, continuum robots have demonstrated interesting potential within a wide scope of uses in hostile environment. They have been used for manipulation, navigation, locomotion, grasping, inspection, search, and repair [1]–[4]. Nevertheless, biological inspiration brought in some way the researchers' interest for medical applications using continuum robots, reviewed in several works including [5]–[8]. Continuum robots are able to navigate inside the human body through natural orifice access (nasal cavity, esophagus, colon, etc.) for minimally invasive surgery. One may take advantage of their smooth and complex shapes added to their dexterity. In addition, the miniaturization potential brought through innovative designs such as concentric tube robots (CTR) [9], downscaling conventional designs as for tendon-driven mechanisms [10], or integration of smart materials enlarges the scope of the considered medical applications. Embedding soft micro-actuators in continuum robots is introduced hereby in contrast with (i) external tendon/cable-actuation that undergo troublesome friction and torsion phenomena and with (i) other intrinsic actuators such as cumbersome pneumatic and hydraulic actuation that sustain integration issues. Moreover, using soft materials is expected to supply additional safety when interacting with human organs [11] due to their reduced stiffness, such as for our target application of an active endomicroscope. Furthermore, actively controlling the curvature of the robot sections liberates from exchanging tubes as proposed in [12]. Electro-Active Polymers (EAP) provide interesting features for the miniaturized actuator in terms of strain, required energy, and biocompatibility [13]. Particularly, the conductive polymers (Polypyrrole, Polyanalinine, Pedot) provide the best characteristics in contrast with the electronic EAP (at least $1kV$ [14], [15]). For example, Polypyrrole (PPy) actuators require very low actuation voltages ($< 2V$) and low currents ($< 1mA$) while generating important strain ($\sim 12\%$) using a thin layer of few microns [16], [17]. Taking advantage of CTR and augmenting them with embedded actuation constitute a promising robotic structure. To the best of our knowledge, the combination of CTR structure and soft micro-actuation – as proposed in [18], modeled and analyzed in [19] – is fabricated and experimented for the first time in this paper.

In this scope, we present a promising paradigm of continuum robots based on the telescopic advantages of the CTR augmented with soft micro-actuators. This novel structure is detailed in section II and modeled kinematically in section III. In section IV, the closed-loop control in 2 Degrees of Freedom (DoF) based on visual servo control and path planning schemes with obstacle avoidance are detailed. Moreover, the novel structure and control schemes are validated experimentally with a developed prototype in section V. Finally, conclusion and future works are drawn.

II. ROBOTIC STRUCTURE

A. Telescopic deployment approach

Based on the outstanding potential of CTR [20], [21], the proposed novel structure takes advantage of the telescopic deployment. In fact, controlling the deployment of the robot is able to protect the end-effector that may carry a sensitive medical tool within the insertion. In the same way, it may protect the human safe tissue from the end-effector that may hold a harmful/sharp tool. To this same aim of safety, reducing the robot size while navigating to the site of interest limits substantially the invasiveness of the procedure. Nevertheless, once the target zone is reached, the robot workspace may be extended when deploying all the sections. All in all, the concentric deployment approach is particularly interesting for medical applications and the robotic structure presented in this paper is based on this paradigm. As demonstrated in [18], [19], [22], actively controlling the curvature of a CTR, as opposed to CTR in the literature, enhances its kinematic performances and enlarges the reachable workspace. In this scope, the telescopic structure is augmented with the PPy soft micro-actuator explained in the following paragraph.

B. Micro-actuator synthesis

In order to augment the CTR approach with a variable curvature, a tri-layer PPy based micro-actuator is developed following prior work of [13]. First, a porous PolyVinylidene Fluoride (PVDF) membrane from Immobilon, Merck

The authors are with the FEMTO-ST Institute, AS2M Department, Univ. Bourgogne Franche-Comté/UFC/CNRS/ENSMM. 24 rue Alain Savary, Besançon, France. mohamed.chikhaoui@femto-st.fr

Millipore Corporation (*http://www.merckmillipore.com/*) of approximately 150 μm thickness and pores of 0.45 μm in diameter is used as a substrate. The latter is sputtered with chromium (Cr) and gold (Au) layers of 40 nm on both sides in order to create the seed layers of the PPy electrodes. Afterwards, the conductive substrate is placed inside a three-electrodes cell containing a platinum (Pt) counter-electrode and a Ag/AgCl reference electrode. The polymerization is performed in the compound solution constituted of the monomer (0.1 M pyrrole), the dopant (Bis-trifluoromethane sulfonimide lithium (LiTFSI) salt, 0.1 M), and the solvent (Propylene carbonate) from Sigma-Aldrich Co. (*http://www.sigmaaldrich.com/*). It is performed using a cyclic voltammetry system at low voltage (0.7 V) and low temperature (-20°C) to control the reaction kinetics and to obtain a compact layer of approximately 10 μm, as demonstrated in [23]. A rectangular part of the actuator (30×2.5 mm) is cut and connected on both sides to the actuation miniaturized gripper (see section V.A for details) and linked to the power supply. When applying a voltage difference on the 2 electrodes of the soaked PVDF/Cr/Au/PPy micro-actuator by the electrolyte solution (LiTFSI), an electro-chemo-mechanical conversion occurs. In fact, the positively powered electrode expands by means of ionic exchange from the electrolyte (oxidation), while the negatively powered electrode retracts by means of the opposite reaction (reduction) as described in Figure 1a. This volume difference produces a bending moment at very low voltages (<2 V) and bending angles up to +/-180° were performed in air. The stress distribution along the micro-actuator is constant and its shape is considered as circular during all the experiments.

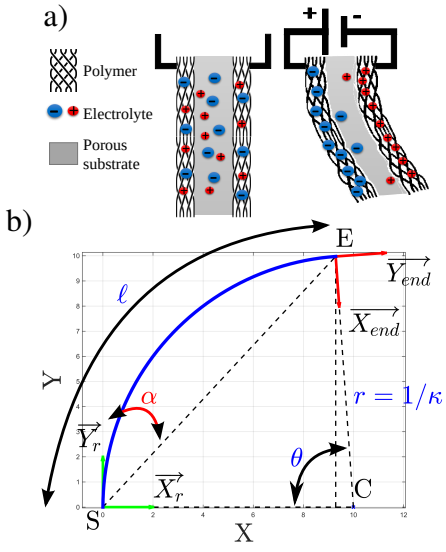

Fig. 1. a) Ionic EAP actuation principle and b) 2D arc schematic description.

III. KINEMATIC MODEL

A. Forward kinematics

The concentric soft robot presented hereby is constituted of a straight section (stiff tube) and a curved section (tri-layer planar PVDF/Cr/Au/PPy micro-actuator) translating within the tube. The forward in-plane kinematic model (FKM) is based on the constant curvature assumption, as validated for the developed micro-actuator. An arc of a circle in the X-Y plane is defined, following Figure 1b, by its curvature κ (inverse of the radius of curvature r) and its length ℓ. Thus, the transformation matrix from the arc origin frame $\left(S, \overrightarrow{X_r}, \overrightarrow{Y_r}\right)$ to its tip frame $\left(E, \overrightarrow{X_{end}}, \overrightarrow{Y_{end}}\right)$ is:

$$ {}^0T_1 = {}^0T_1(\kappa, \ell) = \begin{bmatrix} R_z(\theta) & \mathbf{p} \\ 0 & 1 \end{bmatrix} \quad (1) $$

where $R_z(\theta)$ is the rotation about the $\overrightarrow{Z}$ axis with the bending angle $\theta = \kappa\ell$ and $\mathbf{p} = [r(1-\cos\theta), r\sin\theta]^T$ is the arc tip location. The arc variables κ and ℓ are linked to the robot actuators.

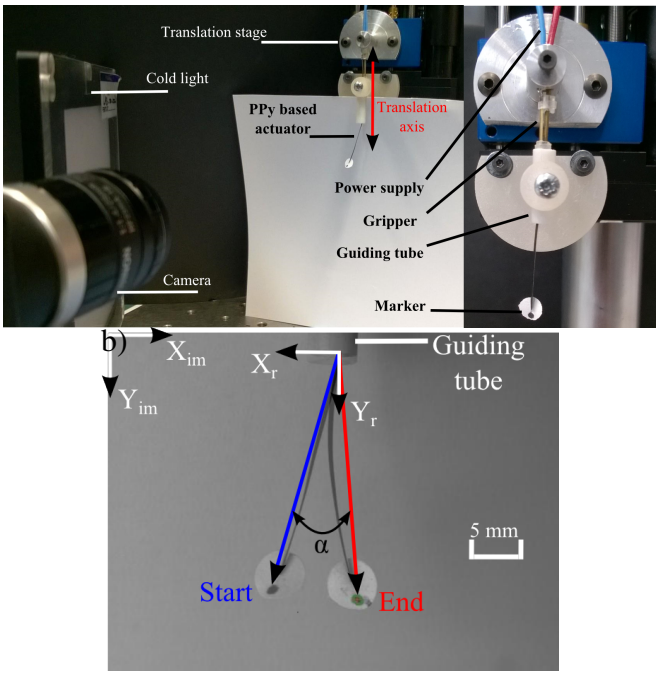

Fig. 2. a) Experimental setup with b) a zoomed image of the micro-actuator at 2 different angular positions when totally deployed. An example of the measured angle α between two actuator positions is depicted.

For the considered robot with 2 sections, the first one is constituted of a fixed straight tube along $\overrightarrow{Y_r}$ axis and the second is the PPy based micro-actuator as described in Figure 2. The latter can translate along the $\overrightarrow{Y_r}$ axis by ρ_2 and bend about the $\overrightarrow{Z}$ axis when its electrodes are supplied by the voltage v_2. Thus, the actuator space is denoted $\mathbf{q} = [\rho_2 \quad v_2]^T$. The intrinsic curvature of the first section is denoted $\kappa_{1_{in}} = 0$ and that of the second section micro-actuator is $\kappa_{2_{in}} = C_{PPy_2} v_2$ noting that C_{PPy_2} is the PPy electro-chemical conversion of the micro-actuator. Thus, the first section parameters are: (i) the curvature $\kappa_1 = 0$ as the micro-actuator stiffness is considered to be negligible compared to that of the tube and (ii) the length $\ell_1 = L_1$ which is constant. The second section curvature is $\kappa_2 = \kappa_{2_{in}}$ as it is free outside the guiding tube and its length is $\ell_2 = \rho_2$.

B. In-plane inverse kinematics

The model is inverted geometrically in order to find a closed-form planar solution and to properly describe the robot end-effector position and shape. Noting that the desired point is denoted $E(x_E, y_E)$ and the start point is S, the arc variables are computed such that:

$$\kappa = \frac{2y_E}{x_E^2 + y_E^2} \tag{2}$$

$$\ell = \begin{cases} \frac{1}{\kappa}\ acos\left(1 - \kappa\ x_E\right) & \text{if} \quad y_E > 0 \\ \frac{1}{\kappa}\left(2\pi - acos\left(1 - \kappa\ x_E\right)\right) & \text{else.} \end{cases} \tag{3}$$

The homogeneous in-plane transformation matrix is then computed such as ${}^0T_1$ in (1). This step is summarized in the IKM function denoted $(\kappa, \ell) = IKM(S, E)$.

This geometrical method provides the desired arc parameters χ_2 leading to exact positioning of the end-effector in simulation at a very high computation speed (ie. computation of (2) and (3)). However, for a realistic use of this method, one must take into account (i) the smooth motion that should be described by the robot in order to reach its target, (ii) the robot reachable set of points, and (iii) the actuator resolutions for the translation movements (telescopic behavior) and the PPy based soft micro-actuator. Thus, problem (i) leads to path generation (or path planning for advanced control). The search of a set of intermediary points between the initial position and the target one is then mandatory in order to supervise the robot behavior. Problem (ii) induces a preliminary test of the target point to validate its location inside the pre-computed robot workspace. Problem (i) should also take into account the constraints of (ii) and compute an admissible path. Finally, the physical behavior of the micro-actuator and the translation stage – namely bending and travel range, respectively – are used to define the realistic workspace and its sampling due to the actuation resolutions to be consistent with constraint (iii).

IV. Closed-loop control and obstacle avoidance

A. Visual servoing of the soft micro-actuator

A final conversion function g is used to transform the IKM curvature output κ to an angular measure between the robot origin $\overrightarrow{Y_r}$ axis (at the clamping point S) and the end-effector position E as described in Figure 1b. Recalling that $\theta = \kappa\ell$ and for a fixed deployed length, g is defined such that:

$$\alpha = g(\theta) = \left(\widehat{\overrightarrow{X_r}, \overrightarrow{Y_r}}\right) - \left(\widehat{\overrightarrow{SC}, \overrightarrow{SE}}\right) = \frac{\theta}{2} \tag{4}$$

One should note that the second term stems from the isosceles triangle CSE at C (Figure 1b). Based on this assumption, the angular measure is performed between the $\overrightarrow{Y_r}$ axis and the robot end-effector at the origin. The visual servoing is then performed following the block diagram on Figure 3. The end-effector position is detected on the image output E which is converted to an angular measure α. Following the difference ϵ_{ang} with the desired angle α_d (after computing g function), the compensator generates the suitable voltage v_{act} to send to the actuator power supply.

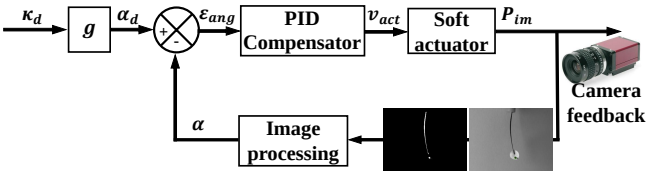

Fig. 3. Block diagram for the visual servoing based curvature control.

B. Path planning

The path planning of the considered telescopic soft robot is performed with respect to the constraints detailed in section III. The path planner (PP) (Figure 4a) can generate an equally spaced set of points. A supplementary step suggests that the latter are tested in contrast with the reachable workspace in order to validate the path.

C. Obstacle avoidance

The obstacle avoidance for the considered medical application is an important issue. Our specific algorithm was tested to achieve a safe control using PP. Once the obstacle is totally defined, the algorithm computes the free-of-collision path offline as globally described in [24]. The tests are performed on the robot shape. The latter is computed using the FKM based on the IKM generated actuator configurations from the planned set of points (Figure 4b). The circular path is enlarged if a collision is predicted and the process is repeated until the condition is fulfilled as mapped in Figure 4c.

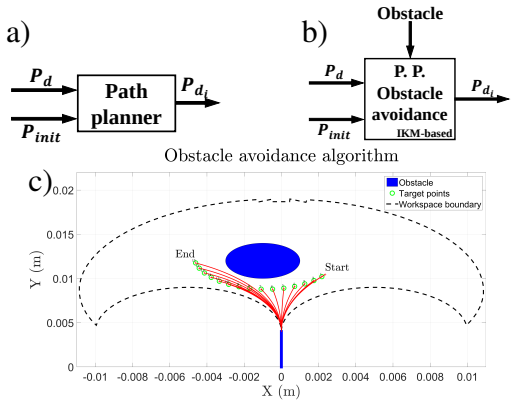

Fig. 4. a) Basic PP scheme and b) PP for obstacle avoidance when the latter is perfectly defined starting from an initial point. c) Simulations of the obstacle avoidance algorithm for a 2 mm–radius obstacle.

D. Position based visual servoing

In practice, the constant curvature assumption used in the modeling turned to be at stake. Thereby, large errors were recorded when using a joint controller based on the use of the IKM. As a consequence, we implemented a visual servo control. To some extent, it belongs to the Position Based Visual Servoing (PBVS) category, since the end-effector position detected in the image is converted into the end-effector position in the robot frame, by (here, simple) geometric considerations. Note that this detection can be addressed

with different eye-to-hand medical imaging systems in an intracorporeal scenario, undergoing the suitable marker. The desired point P_d and the initial point, expressed in the robot frame $(\overrightarrow{X_r}, \overrightarrow{Y_r})$ (cf. Figure 2b), are used in the PP (simple or with obstacle avoidance) to generate the set of points to solve in the control loop. By means of visual feedback, the end-effector position P_{im} in the image frame $(\overrightarrow{X_{im}}, \overrightarrow{Y_{im}})$ is detected and registrated to the robot frame to obtain P. Thus, the positioning error is calculated and the intermediate control $\dot{\mathbf{q}}$ are computed through the kinematic Jacobian inverse J^{-1} that is initialized offline. These variations are integrated through the program sampling time and generate the new desired actuator configurations $\mathbf{q}_d = [\rho_d \ \kappa_d]^T$. Thus, the robot 2 DoF are controlled with inner loops. The translation motor position control is performed in the manufacturer inner loop and the visual servoing of the micro-actuator curvature is executed as previously detailed in section IV.A and Figure 3. The complete control scheme is detailed in Figure 5.

V. EXPERIMENTAL VALIDATION

A. Experimental environment

1) Experimental setup: The voltage controller, the translation stage, and the camera feedback are monitored through a Matlab Simulink program using the Visual Servoing Platform (ViSP: *https://visp.inria.fr/*) through the new opensource dedicated blockset CVLink (*https://sourcesup.renater.fr/cvlink/*). Matlab/Simulink 2011b is ran on an Intel Xeon CPU 2.33 GHz computer.

Tracking the position of the actuator is performed using an IEEE 1394 Guppy FireWire camera (*https://www.alliedvision.com/en/digital-industrial-camera-solutions.html*) placed in front of the smallest dimension of the actuator (hence its thickness) as shown in Figure 2a. The actuator is attached from both sides via a miniaturized conductive gripper. The latter is fabricated from a conductive tube of 1.5 mm diameter and 30 mm length. The tube is then severed longitudinally through electrical discharge machining (wire erosion) using a fine tool-electrode of 100 μm. Therefore, two separate arms are obtained. A heat-shrinkable sleeve of 1 mm length is wrapped around the 2 gripper arms at their middle to unite them and the actuator is properly clamped at one tip. Thus, the required displacement is obtained and the micro-actuator is properly connected. Both of the gripper arms are finally welded to the power wiring.

The voltage is supplied using the USB-6211 National Instruments multifunction data acquisition module (*www.ni.com/*). The 2 analog outputs used to send the voltages can operate between +/-10 V with a resolution of 3.512 mV. One analog input is used to measure the current with a quantum of 0.088 mV through a 10 Ω resistor. On the other side, the gripper is linked to the M111.1DG translation stage from Physik Instrumente with a travel range of 15 mm, a maximum velocity of 1.5 mm/s, and a minimum incremental motion of 0.05 μm using the Mercury C-863 single-axis controller (*http://www.physikinstrumente.com/*). Therefore, the miniaturized conductive gripper and the actuator can translate inside a guiding tube of 5 mm diameter and 20 mm length. The gap between the actuator width and the guiding tube diameter is set in order to prevent capillarity forces to attract the former (immersed in the actuation solution) onto the tube inner wall.

2) Position tracking accuracy: Using the visual feedback, the program detects the actuator by means of a suitable thresholding. In order to track exclusively the actuator end-effector, a physical marker is joined as demonstrated in Figure 2b. It is a circular marker with a dark point of approximately 1 mm diameter (3.5 % of the actuator size) that can be properly detected and tracked by the camera. A preliminary test on the detected mark area is done and an additional evaluation of its shape factor is performed through the isoperimetric quotient (circularity). This test permits a robust tracking of the end-effector during the experiments even when the scene is subject to luminosity variation. The measurement accuracy depends substantially on the marker size. In order to quantify it, the actuator is placed at a static position, and the marker center is detected for an arbitrary duration. Following the calibration of the camera, the variation of the position is detected and converted afterwards to millimeters. The horizontal error of the marker barycenter is about 33 μm while the vertical error is 22 μm.

B. Visual servoing of the soft micro-actuator

The response of the tri-layer micro-actuator end-effector in terms of angular displacement is depicted in Figure 6. A control voltage limitation of 2.5 V was set in order to protect the tri-layer actuator from damage [25].

TABLE I
QUANTITATIVE EVALUATION OF THE ANGULAR RESPONSES

	Steady state error (%)		Tracking error (%)	
Amplitude	Mean	Std	Mean	Std
+/-2°	4.8644	4.0923	8.6948	3.9030
+/-5°	3.7033	1.6378	9.3746	1.5389
+/-10°	2.7731	0.8556	11.9161	0.7146
+/-15°	1.4912	0.3639	9.5468	1.6349
+/-20°	0.2789	0.1275	9.8193	3.3591

The results elucidate the accuracy of the angular control loop with steady state errors lower than 5%. However, the tracking error is non negligible (around 10%). This error is due to the actuator dynamics and can be decreased with an advance component inside the compensator. Thus, this problem can be well-addressed with advanced control theories such that LQG control, H-infinity methods, or full state feedback, among others, but is out of the present scope.

C. Path planning

The experiments were led with the robotic structure such that L_1 = 3.8 mm and concern a single desired point reaching. The control scheme previously presented in Figure 5 was implemented to the considered robot using a sampling time of 0.2 s. This is the minimum admissible by the Matlab/Simulink program with the running processor. The

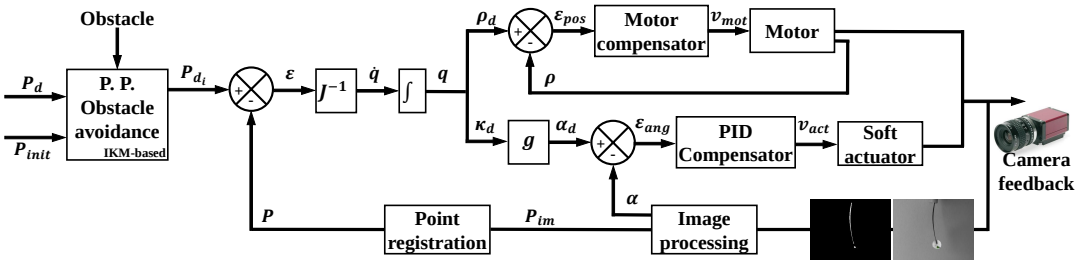

Fig. 5. Block diagram for the complete PBVS scheme of the telescopic soft robot.

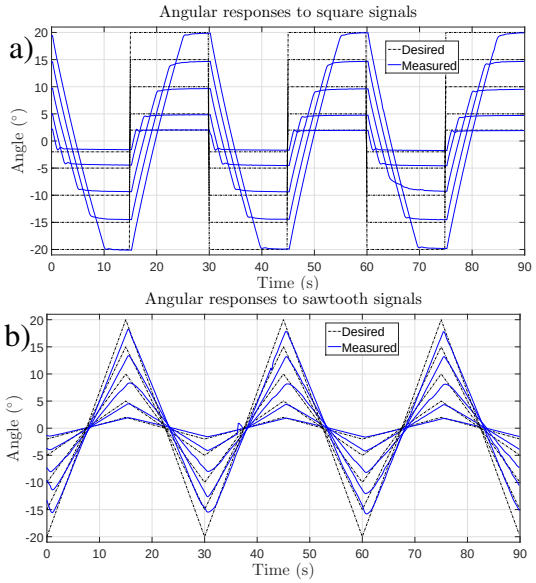

Fig. 6. End-effector angular response with respect to a) a square and b) sawtooth control inputs.

results presented in Figure 7 were obtained for a circular path positioning task with 20 intermediary target points.

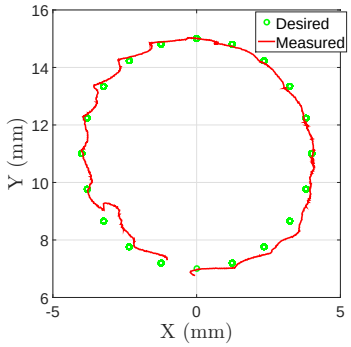

Fig. 7. Achieving a circular path of 4 mm diameter.

These results highlight a positioning accuracy with a mean error of 287.6 μm and a standard deviation of 143.6 μm. Hence, the control scheme with a PP is validated and obstacle avoidance is considered in the following.

D. Obstacle avoidance

The experiments were also led to achieve obstacle avoidance tasks based on the PBVS scheme previously validated with PP. Indeed, an obstacle of 4 mm in diameter is virtually placed on the image at a known location. Following the initial pose and the obstacle registration into the robot frame, the algorithm is ran offline and the generated path is set. Two tests were led with (i) different proportional gains in the curvature servoing loop and (ii) different switching times between the desired intermediary points. The results are depicted in Figure 8.

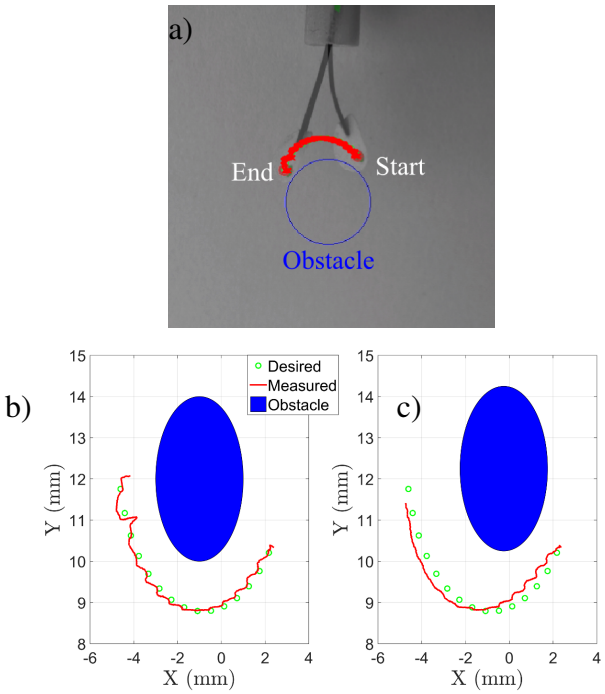

Fig. 8. Obstacle avoidance schemes with: Test 1 (proportional controller P in the curvature servoing loop and switching time S_t) a) on the image and b) in the robot frame. c) Test 2 in the robot frame (proportional controller $2.5P$ and switching time $S_t/2$).

The robot reaches the target following a circular path while keeping a secure distance from the obstacle in both cases. The mean positioning error is 210 μm and its standard deviation is 225 μm throughout the path in the first test, while they are 366 μm and 310 μm for the second test. The considered soft concentric robot is able to achieve faster positioning tasks when tuning the suitable compensator

configurations. Indeed, the tasks in test 2 were performed 2 times faster than those in test 1 for a higher proportional gain. However, this can alter the positioning accuracy with some significant amount (46% more accuracy for test 1) and possibly induce an overshoot. For instance, for the considered obstacle avoidance task, the overshoot is not acceptable as a collision might occur. In contrast, for a fast scanning scheme, the response time should be emphasized which leads to the use of higher gains in the control loop. Hence, following the specifications of the target application, the safety requirements, and the environment constraints, one can determine the relevant feature to underline.

VI. CONCLUSIONS

The telescopic tube paradigm augmented with PPy based soft micro-actuator was realized for the first time in this paper. The 2D forward and inverse kinematics were derived and validated experimentally. The experiments were led following a closed-loop control based on PBVS and performing path planning schemes for an obstacle avoidance. The performances were satisfactory with angular errors below 5% for the curvature visual servo and positioning errors of 287.6 μm for a circular path planning and of 210 μm for the obstacle avoidance in a PBVS scheme. Hence, combining a rigorous modeling of the actuator, a suitable fabrication process, and a reliable controller merging PBVS, one can enhance the performance of these promising technologies.
As a future challenge, the full 3D inverse-kinematics need to be computed to solve for the whole space positioning to enlarge the scope of the potential applications of the proposed structure. The integration within a full CTR is also to be considered with the deposition of 4 antagonistic PPy micro-actuators on a flexible tube. This configuration was previously suggested by [26] and [19] and offers 2 DoF for each tube. In fact, the PPy based micro-actuator generated enough force to bend Silicone tube of 1 mm diameter in 2 orthogonal directions. The major advantage is that the robot lumen is released in order to house additional tools. For instance, optical fibers can be inserted and a scanning might be performed.

ACKNOWLEDGMENT

The authors would like to thank Guillaume Laurent for his support with the CVLink libraries. This work has been supported by the Labex ACTION project (contract ANR-11-LABX-0001-01) and by NEMRO project (contract ANR-14-CE17-0013).

REFERENCES

[1] S. Hirose, *Biologically inspired robots : snake-like locomotors and manipulators / Shigeo Hirose ; translated by Peter Cave and Charles Goulden*. Oxford University Press Oxford ; New York, 1993.

[2] G. Robinson and J. Davies, "Continuum robots - a state of the art," in *IEEE International Conference on Robotics and Automation*, vol. 4, 1999, pp. 2849–2854.

[3] M. Toda. (2015, Feb) Japan readies first robot to probe melted fukushima reactor. Phys. Org. The Associated Press. [Online]. Available: http://phys.org/news/2015-02-japan-readies-robot-probe-fukushima.html

[4] A. Wolf and H. Brown et al., "A mobile hyper redundant mechanism for search and rescue tasks," in *IEEE/RSJ International Conference on Intelligent Robots and Systems*, vol. 3, 2003, pp. 2889–2895.

[5] D. Trivedi, C. D. Rahn, W. M. Kier, and I. D. Walker, "Soft robotics: Biological inspiration, state of the art, and future research," *Applied Bionics and Biomechanics*, vol. 5, no. 3, pp. 99–117, 2008.

[6] R. J. Webster III and B. A. Jones, "Design and kinematic modeling of constant curvature continuum robots: A review," *International Journal of Robotics Research*, vol. 29, pp. 1661–1683, 2010.

[7] S. Kim, C. Laschi, and B. Trimmer, "Soft robotics: a bioinspired evolution in robotics," *Trends in Biotechnology*, vol. 31, no. 5, pp. 287–294, Apr 2013.

[8] J. Burgner-Kahrs, D. Rucker, and H. Choset, "Continuum robots for medical applications: A survey," *IEEE Transactions on Robotics*, vol. 31, no. 6, pp. 1261–1280, Dec 2015.

[9] P. Sears and P. Dupont, "A steerable needle technology using curved concentric tubes," in *IEEE/RSJ International Conference on Intelligent Robots and Systems*, Beijing, China, Oct 2006, pp. 2850–2856.

[10] D. B. Camarillo and C. F. Milne et al., "Mechanics modeling of tendon-driven continuum manipulators," *IEEE Transactions on Robotics*, vol. 24, no. 6, pp. 1262–1273, 2008.

[11] R. J. Wood and C. J. Walsh, "Smaller, softer, safer, smarter robots," *Science Translational Medicine*, vol. 5, no. 210, p. 210ed19, 2013.

[12] J. Burgner, P. Swaney, R. Lathrop, K. Weaver, and R. J. Webster III, "Debulking from within: A robotic steerable cannula for intracerebral hemorrhage evacuation," *IEEE Transactions on Biomedical Engineering*, vol. 60, no. 9, pp. 2567–2575, Sep 2013.

[13] G. M. Spinks, T. E. Campbell, and G. G. Wallace, "Force generation from polypyrrole actuators," *SPIE Smart Materials and Structures*, vol. 14, no. 2, p. 406, 2005.

[14] F. Ganet, M. Q. Le, J. F. Capsal, P. Lermusiaux, L. Petit, A. Millon, and P. J. Cottinet, "Development of a smart guide wire using an electrostrictive polymer: option for steerable orientation and force feedback," *Scientific Reports*, vol. 5, no. 18593, Dec 2015.

[15] G. Kovacs, L. Dring, S. Michel, and G. Terrasi, "Stacked dielectric elastomer actuator for tensile force transmission," *Sensors and Actuators A: Physical*, vol. 155, no. 2, pp. 299 – 307, 2009.

[16] G. Spinks and B. Xi et al., "In pursuit of high-force/high-stroke conducting polymer actuators (invited paper)," *SPIE Smart Structures and Materials*, vol. 5759, pp. 314–321, 2005.

[17] G. Alici and N. Huynh, "Performance quantification of conducting polymer actuators for real applications: A microgripping system," *IEEE/ASME Transactions on Mechatronics*, vol. 12, no. 1, pp. 73–84, Feb 2007.

[18] M. T. Chikhaoui, K. Rabenorosoa, and N. Andreff, "Kinematic modeling of an EAP actuated continuum robot for active micro-endoscopy," in *Advances in Robot Kinematics*, J. Lenarčič and O. Khatib, Eds. Springer International Publishing, 2014, pp. 457–465.

[19] ——, "Kinematics and performance analysis of a novel concentric tube robotic structure with embedded soft micro-actuation," *Mechanism and Machine Theory*, vol. 104, pp. 234 – 254, 2016.

[20] H. Gilbert and R. J. Webster III, "Can concentric tube robots follow the leader?" in *IEEE International Conference on Robotics and Automation*, Karlsruhe, Germany, May 2013, pp. 4881–4887.

[21] A. W. Mahoney, H. B. Gilbert, and R. J. Webster III, *A Review of Concentric Tube Robots: Modeling, Control, Design, Planning, and Sensing*, In Press, vol. Minimally Invasive Surgical Robotics.

[22] M. T. Chikhaoui, K. Rabenorosoa, and N. Andreff, "Towards clinical application of continuum active micro-endoscope robot based on EAP actuation," in *Surgetica*, Chambéry, France, Dec 2014.

[23] A. Cot, M. T. Chikhaoui, P. Rougeot, K. Rabenorosoa, and N. Andreff, "Synthesis, encapsulation, and performance analysis of large deformation tri-layer polypyrrole actuator," in *IEEE International Conference on Advanced Intelligent Mechatronics*, Banff, Canada, Jul 2016, pp. 436–441.

[24] S. Y. Nof, *Handbook of industrial robotics*. John Wiley & Sons, 1999, vol. 1.

[25] J. D. Madden, *Electroactive Polymers for Robotic Applications: Artificial Muscles and Sensors*. Springer London, 2007, ch. Polypyrrole Actuators: Properties and Initial Applications, pp. 121–152.

[26] T. Shoa and J. Madden et al., "Conducting polymer based active catheter for minimally invasive interventions inside arteries," in *IEEE Engineering in Medicine and Biology Society*, 2008, pp. 2063–2066.